STUDIA UBB CHEMIA, LXV, 1, 2020 (p. 177-188)
(RECOMMENDED CITATION)
DOI:10.24193/subbchem.2020.1.14

SYNTHESIS AND CHARACTERISATION OF Fe_3O_4-SnO_2 NANOCOMPOSITES WITH ELECTROCHEMICAL PROPERTIES

SERGIU MACAVEI[a], MARIA ŞTEFAN[a*], FLORINA POGACEAN[a], OVIDIU PANĂ[a], CRISTIAN LEOSTEAN[a], ADRIANA POPA[a], DANA TOLOMAN[a], LUCIAN BARBU-TUDORAN[a]

ABSTRACT. Composite Fe_3O_4-SnO_2 nanoparticles were synthesized by growing SnO_2 nanoparticles on the surface of previously prepared Fe_3O_4 nanoparticles. First, Fe_3O_4 nanoparticles were prepared by chemical precipitation of precursors followed by the obtaining of SnO_2 nanoparticles by chemical precipitation or sol-gel process. The composite nanoparticle samples were characterized by using X-Ray diffraction (XRD), Transmission Electron Microscopy (TEM) and X-Ray photoelectron Spectroscopy (XPS) techniques. Also, electrochemical behaviour was recorded. The results revealed that by adjusting the composition of components one can control the properties of composite nanoparticles.

Keywords: *SnO_2; nanoparticles; photocatalytic properties, electrochemical properties*

INTRODUCTION

For the past several decades, studies of nanometer-sized materials have attracted a considerable attention due to their unique optical, electrical, physical, chemical, and magnetic properties [1-4]. Since the current investigated materials are limited in terms of properties, price and multifunctionality, the increasing need of new nanostructured composite materials for different applications is become critical due to rapid growing of this market [5-7].

The composite nanostructures with different architecture like core-shell do not simply combine properties of the original components but also possess novel and collective performances which are not seen in the original

[a] *Institute for Research and Development of Isotopic and Molecular Technologies, Donath Str.67-103, RO-400293 Cluj-Napoca, Romania*
* *Corresponding author: mstefan@itim-cj.ro*

constituents. Physical and chemical properties of nanostructured composite materials can be adjusted by controlling the composition and the relative sizes of various components [8-11].

In this regard, combining the properties of Fe_3O_4 and SnO_2 a novel composite nanostructure with morpho-structural and magnetic properties in one single entity was obtained. These properties of Fe_3O_4-SnO_2 composite nanostructure would greatly broaden their application in photocatalysis [12,13], Li-ion batteries (LIBs) [14,15], magnetic resonance imaging (MRI) [16], sensors and biosensors [17], etc.

From a large variety of metal oxides, special attention has been paid to oxides of the Fe_3O_4, SnO_2 and their combinations due to their good electrochemical capacitance low cost and their positive impact on the environment [18,19].

The paper aims to report the synthesis and morpho-structural characterisation of Fe_3O_4-SnO_2 nanocomposites. The electrochemical properties were also evidenced.

RESULTS AND DISCUSSION

The X-ray diffraction analysis of the synthesized sample was performed in order to identify the crystal structure and to estimate average crystallite size. In figure 1 are presented the XRD pattern of the samples with different Fe_3O_4:SnO_2 molar ratio.

The diffraction planes (220), (311), (400), (511), (440) of Fe_3O_4 (JCPD 99-100-2343) was identified.

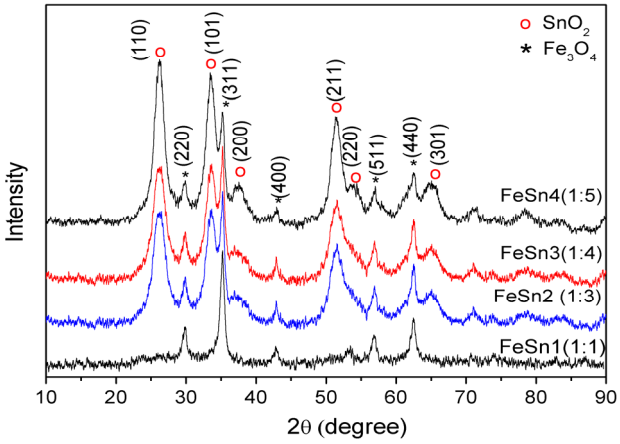

Figure 1. XRD diffraction patterns and corresponding indexation of SnO_2-Fe_3O_4 samples with different molar ration between the two components.

By increasing the SnO_2 content diffraction peaks at 2θ = 26.11, 33.58, 37.56, 51.26, 52.53, 64.96 corresponding to (110), (101), (200), (211), (220), (301) planes for rutile type tetragonal structure of SnO_2 can be observed. The intensity of these peaks increases with the increase of SnO_2 content.

The average crystallites sizes were calculated with Scherrer equation by using diffraction peaks related to the planes (220) for Fe_3O_4 and (110) for SnO_2 and a size of 12.5 nm and 5 nm was obtained for Fe_3O_4 and SnO_2 crystallites, respectively.

The morphology of Fe_3O_4-SnO_2 nanocomposites was determined by transmission electron microscopy (TEM). As an example, the TEM image for FeSn2 sample with corresponding size distribution is shown in Figure 2. The larger Fe_3O_4 cores are embeded in a berry structure of SnO_2 smaller nanoparticles. The particle size distribution for FeSn2 sample (inset of figure 2) shows two maxima distribution. The dotted line represents the best fit realized by using a superposition of two lognormal distribution functions. The obtained mean diameters 6.8 and 12.3nm are in agreement with XRD results and are attributed to SnO_2 and Fe_3O_4.

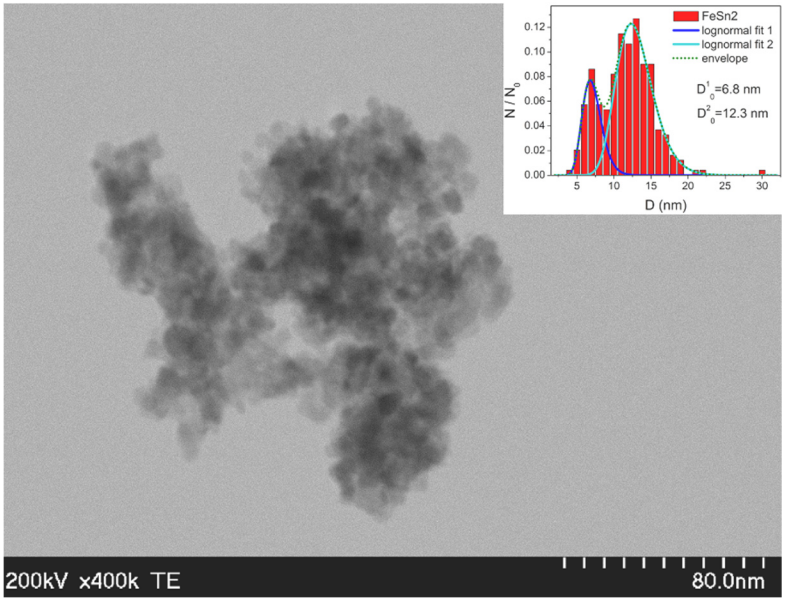

Figure 2. TEM image of FeSn2 sample together with corresponding size distribution

The high-resolution TEM (HRTEM) image of Fe_3O_4-SnO_2 sample is given in figure 3. Lattice fringes are clearly visible in images revealing the crystalline nature of nanoparticles. Based on the Fourier Transform analysis, the interplanar distances were atribued to crystalline phases of Fe_3O_4 and SnO_2. As one can see in the inset of figure 3, the reciprocal lattice points for Fe_3O_4 (111) and SnO_2 (301), SnO_2 (101), SnO_2 (111), SnO_2 (110), SnO_2 (211) were found in the square marked area.

For quantitative analysis of samples the following XPS core-level lines were recorded: Fe 3*p*, Sn 3*d*, O 1*s* and C 1*s*. The C 1*s* line associated to C-C or C-H bindings positioned at 284.6 eV was used for spectra calibration. A Shirley background was used for the deconvolution.

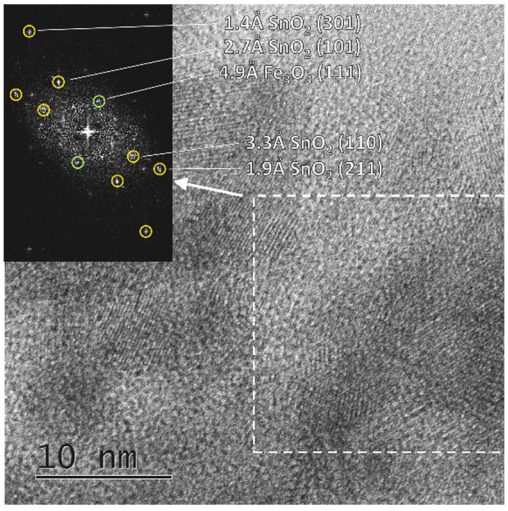

Figure 3. HRTEM image corresponding to FeSn1 sample. Fourier transform (inset) of marked square area reveal the presence of Fe_3O_4 and SnO_2.

For qualitative analysis the XPS survey spectrum of FeSn2 sample is shown in Figure 4a. One can see that only the expected elements are observed: Sn, Fe and O. The small C 1*s* peak is attributed to adventitious carbon.

The XPS spectrum together with the corresponding deconvolutions of Sn 3*d* core-level for FeSn2 sample is presented in figure 4b. The deconvoluted features represent the Sn atoms in (4^+) oxidation states. Besides the main lines, two sets of satellite peaks are also seen in all spectra.

The XPS Fe 3*p* core-level spectrum for FeSn2 sample is presented in Figure 4c. The deconvoluted features represent the Fe atoms in (3^+) and (2^+) oxidation states with the corresponding 2:1 ratio for Fe_3O_4.

The core-shell architecture of nanoparticles was investigated by XPS depth profile analysis. It was performed by using Ar ions etching with 1000 V and 10 mA filament current.

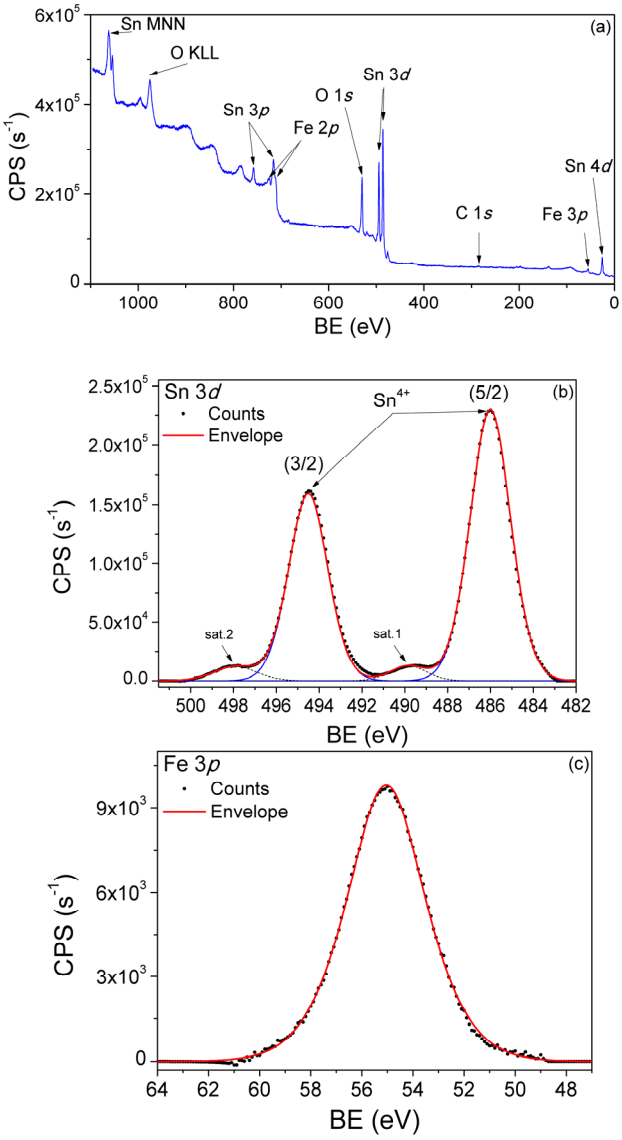

Figure 4. (a) XPS survey spectrum of FeSn2 sample; XPS spectrum together with the corresponding deconvolutions of (b) Sn 3*d* core-levels;(c) Fe 3*p* core-level.

In figure 5 one can see that the intensity of the Sn 3*d*(5/2) line decrease while the intensity Fe 3*p* lines (core) increase. This is an indication of core-shell structure formation.

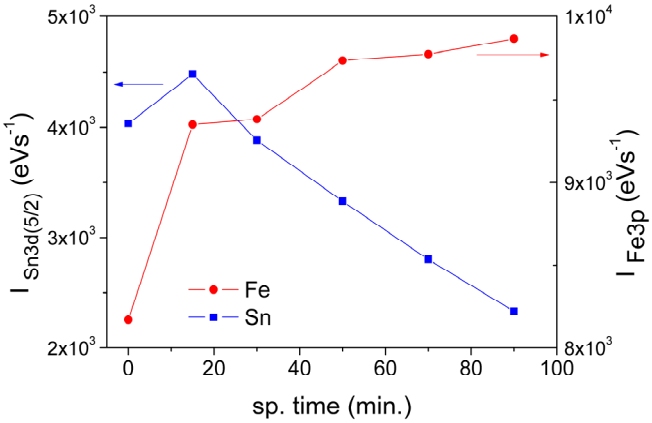

Figure 5. Variation of Sn^{4+} 3p(3/2) and Fe 3p core-level lines as a function of sputtering time

The electrochemical behavior of the electrodes containing Fe_3O_4-SnO_2 nanocomposites has been investigated by using cyclic voltammetry performed at different scan rates and testing their stability at multiple cycling.

Electrochemical response of paste electrodes obtained from FeSn1 sample and graphite using the aqueous solution of LiCl 1M as support electrolyte are shown in figure 6 (a and b).

Cyclic voltammograms reveal the existence of well-defined redox couples corresponding to both Fe_3O_4 and SnO_2 even at low scan rates. Also, the anodic peaks (Ep_a) and the cathodic peak (Ep_c) intensity were measured. Thus, for scan rates 2 mV, the oxidation potential is at 0.13V, while higher than 10 mV the potential value is shifted to 0.70V (figure 6b). The intensities of the redox peaks increase with the number of cycles indicating that the presence of the two reactive species in FeSn1 sample improve the electrochemical response of the material. The electrochemical stability FeSn1 is shown in figure 6a. The good stability of Fe_3O_4-SnO_2 nanocomposites at multiple cycles (50 at high scan speed (100mV) was observed.

Possible electrochemical reactions during the intercalation/extraction process of Li^+ ions for FeSn1 nanocomposites can be described by the following reactions.

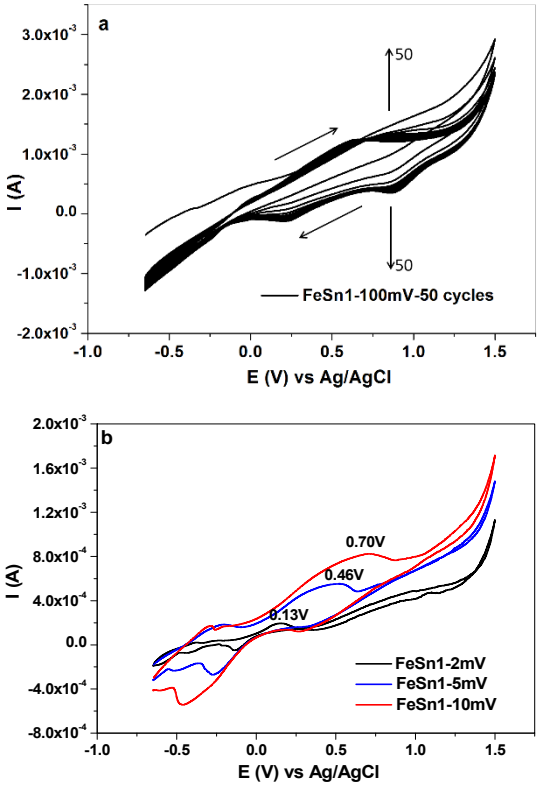

Figure 6. Cyclic voltammograms recorded with FeSn1 paste electrode in LiCl 1M electrolytes: a) Stability testing (50 cycles, scan rate 100mV/s); b) variation of scanning rates from 2 -10 mV/s.

$$Fe_3O_4 + 2Li^+ + 2e^- \rightarrow Li_2(Fe_3O_4) \quad (1)$$

$$Li_2(Fe_3O_4) + 6Li^+ + 6e^- \rightarrow 3Fe + 4Li_2O \quad (2)$$

$$Fe + 4Li_2O \rightarrow Fe_3O_4 + 8Li^+ + 8e^- \quad (3)$$

Regarding the samples with high content of SnO_2, FeSn3 electrochemical stability was tested by cycling electrodes in 1 M LiCl, for 50 cycles at a scanning speed of 100 mV / s (figure 7).

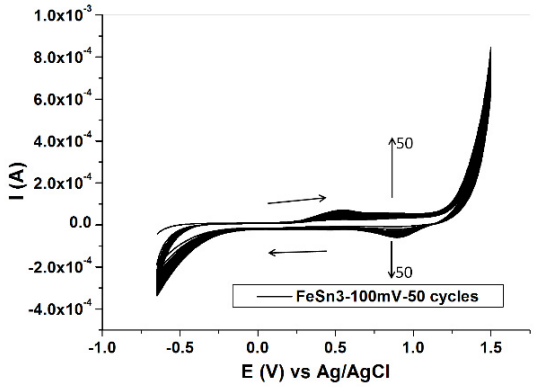

Figure 7. Cyclic voltammograms recorded with FeSn3 paste electrode, in LiCl 1 M electrolytes; Stability testing (50 cycles, scan rate 100mV/s).

The cyclic voltammograms presented show that through repeated cycling in the LiCl 1 M electrolytes, the oxidation and reduction peaks increase due to adsorption on the surface electrode of different electrochemical species.

In the specific case of sample FeSn3, the concentration of Fe_3O_4 in the composite being reduced (the molar ratio between Fe_3O_4 and SnO_2 is 1: 3), the intensity of the oxido-reduction peaks related to the intercalation-de-intercalation of Li^+ ions in Fe_3O_4 decreases or is even absent at low scanning speeds.

The same behavior is observed for FeSn4 samples. The cyclic voltamograms corresponding to FeSn4 sample in LiCl 1 M aqueous solution as electrolyte support was presented in figure 8.

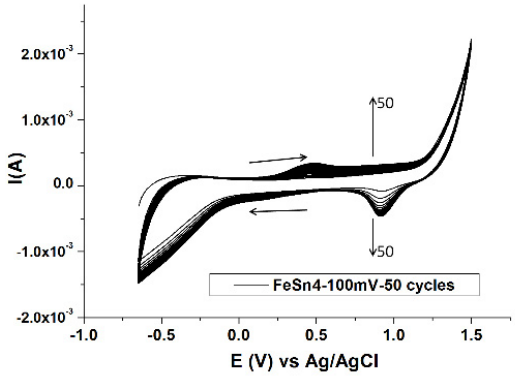

Figure 8. Cyclic voltammograms recorded with $FeSn_4$ paste electrode in LiCl 1 M electrolytes;Stability testing (50 cycles, scan rate 100mV/s).

Cyclic voltammeters occur with increasing oxidation and reduction peaks intensity involved in the reversible processes at electrode. This behavior demonstrates the good electrochemical performance of electrode material based on FeSn1 sample (molar ratio Fe_3O_4:SnO_2= 1:1). The composition and structure of the investigated electrode materials plays an important role in the oxidation-reduction processes at the electrode. The increasing the quantity of SnO_2 in composite samples relative to the amount of Fe_3O_4 seems to have no effect on electrochemical response of nanocomposites.

EXPERIMENTAL SECTION

Materials

The chemical reagents used for the preparation of Fe_3O_4-SnO_2 composite nanoparticles are: $FeCl_3$ x $6H_2O$ (98% Alfa Aesar), $FeCl_2$ x $4H_2O$ (98% Alfa Aesar), NH_3 (25% Merck), sodium laurylsulphate-SLS (p.a Fluka) tin cloride $SnCl_2$ x $2H_2O$ (for synthesis, Merck), sodium hydroxide (98% Alpha Aesar), graphite powder (99.99%, Sigma-Aldrich). $LiNO_3$ (98% Chemapol), LiCl (for synthesis, Merck), silicone oil (Sigma-Aldrich). All chemicals are analytical grade without further purification and were used as received.

Sample preparation

The Fe_3O_4-SnO_2 nanocomposites were prepared by precipitation seed mediated growth onto preformed magnetite nanoparticles [20, 21]. The magnetite nanoparticles were obtained by chemical precipitation. Next, SnO_2 nanocrystals were obtained by precipitation method performed by adding the reagents one-into-another via reagent sequential addition technique (S*eqAdd*) to form Fe_3O_4-SnO_2 nanocomposites. The details of experimental procedure are presented as follows. In the first stage, magnetite nanoparticles were redispersed in bidistilled water 1 h, then in aqueous solution of sodium laurylsulphate (SLS) (0.6 mMol) to prevents the aggregation of Fe_3O_4 nanoparticles due to the steric repulsion, under vigorous stirring at room temperature for 12 h. The as treated magnetite particles were separated and then redispersed in 100 ml $SnCl_2x2H_2O$ (0.70÷3.2 mMol) aqueous solution under continuous stirring for 24 h. Further 100 ml NaOH (1.4÷6.4 mMol) aqueous solution was drop wise added to the mixture. After the addition of NaOH was finished, the reaction was kept 4 hours under vigorous stirring. The as prepared Fe_3O_4-SnO_2 nanocomposite were magnetically collected and washed with water and ethanol (1:1 v/v) for several times to remove the excess of reactants and then dried at 65^{o}C, in air.

Finally, the dried and homogenized samples were thermally treated for 2h at 600°C in furnace, at a rate of 5°C/min, in order to get the Fe_3O_4-SnO_2 composite nanoparticles. In order to evidenced the influence of SnO_2 content on the morpho-structural and electrochemical characteristics of Fe_3O_4-SnO_2 nanocomposites, a series of samples with different Fe_3O_4:SnO_2 molar ratios were prepared, as following: 1:1 (FeSn1), 1:2 (FeSn2), 1:3 (FeSn3) and 1:4 (FeSn4).

Samples characterization

The crystalline structure of samples was evidenced by X-ray diffraction (XRD), recorded by using a Bruker D8 Advance X-ray diffractometer set-up, at 40 kV and 40 mA equipped with a germanium monochromator in the incident beam. The X-ray diffraction patterns were collected in a step-scanning mode with steps of $\Delta\theta = 0.02°$ using Cu Kα1 radiation ($\lambda = 1.54056$ Å) in the 2θ range 10°-80°. Pure silicon powder was used as standard for instrument broadening correction.

Transmission electron microscopy (TEM) was carried out to determine morphology of the nanocomposites. The TEM measurements were performed with Hitachi SU8230 Transmission Electron Microscope equipped with a cold field emission gun. The powder were dispersed in ethanol, with a BANDELIN SONOREX homogenizer and deposited on 400 meshes copper grid, which was coated with carbon film. The HRTEM images were collected with Hitachi H9000NAR transmission electron microscope.

The qualitative and quantitative compositions of samples were investigated by using X-Ray Photoelectron Spectroscopy (XPS) assisted by Ar ions etching. The XPS spectra were recorded by using a SPECS spectrometer working with Al anode (1486.6 eV) as X-rays source. XPS depth profile analysis was performed by using Ar ions etching with 1000 V and 10 mA filament current.

The electrochemical measurements (Cyclic Voltammetry-CV) were performed with an Autolab 302N Potentiostat/Galvanostat (Metrohm Autolab B.V., Utrecht, the Netherlands) connected to a three-electrode cell and controlled by Nova1.11 software and a personal computer. A paste electrode with graphite and nanocomposite Fe_3O_4-SnO_2 was used as working electrode, Pt electrode was employed as counter-electrode, and Ag/AgCl electrode was used as reference.

The electrochemical experiments were carried out in electrolyte solutions of LiCl 1M with different scan rate (2, 5, 10 mV/s) were typically recorded between -0.5 and +1.5 V vs Ag/AgCl.

The paste electrodes were prepared by adding silicon oil into the composite materials containing Fe_3O_4-SnO_2 and mixing them into an agate mortar, until a uniformly wetted paste was obtained. The obtained paste was

mix with two parts of graphite and then packed in a PVC tube (3 mm internal diameter and 5 cm long). A copper disk inserted into the electrode paste to ensure the electrical contact.

CONCLUSIONS

Fe_3O_4-SnO_2 nanocomposites with different ratio of components were prepared in two stages by growing SnO_2 onto preformed Fe_3O_4 nanoparticles. XRD investigations evidenced the presence of crystalline Fe_3O_4 and SnO_2. The crystallite size of 12.5 nm and 5 nm was obtained for Fe_3O_4 and SnO_2 crystallites, respectively.

The TEM/HRTEM investigation shows that the 12.3 nm Fe_3O_4 cores are embedded in a berry structure of 6.8 nm SnO_2 nanoparticles. XPS investigations show the qualitative compositions of samples and oxidation state Sn^{4+} (SnO_2) and Fe^{2+}/Fe^{3+} (Fe_3O_4) in the samples. The formation of the core shell structure was investigated by depth profile evolution of Sn 3*d* and Fe 3p core-levels XPS lines. The electrochemical behavior was evidenced on paste electrodes containing Fe_3O_4-SnO_2 nanocomposites. The results indicate the excellent rate capability and a significantly enhanced cyclic performance depending on composition of electrode material. The increasing oxidation and reduction peaks intensity involved in the reversible processes at electrode demonstrates the good capability of samples to be used as anodes in Li-ion batteries. Further researches are needed to establish optimized synthesis parameters for the electrode material and a complex electrochemical characterization.

ACKNOWLEDGEMENTS

The authors would like to express appreciation to the Ministry of Education and Research for the financial support through Project PN 19 35 02 03 (Core Program).

REFERENCES

1. J. Chang, J. Ma, Q. Ma, D. Zhang, N. Qiao, M. Hu, H. Ma, *Appl. Clay Sci.,* **2016**, *119*, 132-133.
2. R. Li, X. Ren, F. Zhang, C. Du, J. Liu, *Chem. Commun.*, **2012**, *48*, 5010-5012.
3. H. J. Zhang, G. H. Chen, D. W. Bahnemann, *J. Mat. Chem.*, **2009**, *19*, 5089-5121.
4. N. Du, Y. F. Chen, C. X. Zhai, H. Zhang, D. Yang, *Nanoscale*, **2013**, *5*, 4744-4750.

5. X. N. Zheng, X. Y. Yin, B. Wang, M. G. Ma, *Sci. Adv. Mat.,* **2020**, *12*, 613-627.
6. R. G. Chaudhuri, S. Paria, *Chem. Rev.,* **2012**, *112*, 2373-2433.
7. C. Song, Z. Ye, G. Wang, J. Yuan, Y. Guan, *ACS Nano,* **2010**, *4*, 5389-5387.
8. W. Wu, S. Zhang, F. Ren, X. Xiao, J. Zhou, C. Jiang, *Nanoscale*, **2011**, *3*, 4676-4684.
9. J. U. Hur, J. S. Han, J. R. Shin, H. Y. Park, S. C. Choi, Y-G. Jung, G. S. An, *Ceram. Int*., **2019**, *45*, 21395-21400.
10. J. Jiang, Y. Y. Li, J. P. Liu, X. T. Huang, C. Z. Yuan, X. W. Lou, *Adv. Mater.,* **2012**, *24*, 5166-5180.
11. C. Karunakaran, S. S. Raadha, P. Gomathisankar, P. Vinayagamoorthy, *Powder Technol*., **2013**, *246*, 635-642.
12. V. M. Vinosel, S. Anand, Y. A. Janifer, S. Pauline, S. Dhanavel, P. Pravvena, A. Stephen, *J. Mat. Sci. Mater. Electron.*, **2019**, *30*, 9663-9677.
13. D. Chu, J. Mo, Q. Peng, Y. P. Zhang, Y. G. Wei, Z. B. Zhuang, Y. D. Li, *Chem. Cat. Chem*., **2011**, *3*, 371-377.
14. R. Li, X. Ren, F. Zhang, *Chem. Com*., **2012**, *48*, 5010-5012.
15. X. Chai, C. Shi, E. Liu, *Appl. Surf. Sci*., **2016**, *361*, 1-10.
16. W. W. Wang, J. L. Yao, *J. Phys. Chem. C*, **2009**, *113*, 3070-3075.
17. H. Bagheri, N. P. Jamali, S. Amidi, A. Hajian, H. Khoshsafar, *Microchem. J.,* **2017***, 131*, 120-129.
18. A. Mehdinia, M. Jebeliyan, T. B. Kayyal, A. Jabbari, *Microchim. Acta,* **2017**, *184*, 707-713.
19. Y. K. Wang, H. Y. Zhang, R. Z. Hu, J. W. Liu, T. van Ree, H. H. Wang, L. C. Yang, M. Zhu, *J. Alloy Compd.,* **2017**, *693*, 1174-1179.
20. C. Leostean, O. Pana, M. Stefan, A. Popa, D. Toloman, M. Senilă, S. Gutoiu, S. Macavei, *Appl. Surf. Sci.,* **2018**, *427,* 192-201.
21. M. Stefan, A. Popa, O. Pană, C. Leostean, D. Toloman, D. Lazar, F. Pogăcean, S. Macavei, S. Gutoiu, *J. Mat. Sci.: Mater. Electron.,* **2018**, *29,* 14132-14143.